JGR Space Physics

RESEARCH ARTICLE
10.1029/2019JA027750

**Key Points:**
- The effect of protons in whistler lower hybrid resonance reflection is verified with two-dimensional full-wave simulation
- In the lower hybrid resonance reflection region, whistler waves become quasi-electrostatic, accompanied with standing wave structure and wave polarization change from circular to linear
- Localized density irregularities off the equator can produce quasi-parallel whistler waves and thus avoid magnetospheric reflection

**Correspondence to:**
L. Chen, and C. Zhou,
lunjin.chen@gmail.com;
chenzhou@whu.edu.cn

**Citation:**
Xu, X., Chen, L., Zhou, C., Liu, X., Xia, Z., Simpson, J. J., & Zhang, Y. (2020). Two-dimensional full-wave simulation of whistler mode wave propagation near the local lower hybrid resonance frequency in a dipole field. *Journal of Geophysical Research: Space Physics*, *125*, e2019JA027750. https://doi.org/10.1029/2019JA027750

Received 24 DEC 2019
Accepted 15 MAR 2020
Accepted article online 25 MAR 2020

©2020. American Geophysical Union. All Rights Reserved.

# Two-Dimensional Full-Wave Simulation of Whistler Mode Wave Propagation Near the Local Lower Hybrid Resonance Frequency in a Dipole Field

**Xiang Xu[1,2], Lunjin Chen[2], Chen Zhou[1], Xu Liu[2], Zhiyang Xia[2], Jamesina J. Simpson[3], and Yuannong Zhang[1]**

[1]Department of Space Physics, School of Electronic Information, Wuhan University, Wuhan, China, [2]William B. Hanson Center for Space Sciences, University of Texas at Dallas, Richardson, TX, USA, [3]Department of Electrical and Computer Engineering, University of Utah, Salt Lake City, UT, USA

**Abstract** We investigate the propagation of whistler mode waves near the local lower hybrid resonance (LHR) frequency in a dipole field with a two-dimensional full-wave model. First, we run a simulation in which a parallel whistler with frequency above the local LHR frequency is launched at the equatorial region in electron plasma. We find that whistler emission propagates along the dipole field line to a high latitude, turns quasi-electrostatic where the wave frequency is close to the local LHR frequency, and continues to propagate until being absorbed. Then, the proton response is considered. We find that (1) a quasi-electrostatic whistler reflects where the wave frequency is below the local LHR frequency and propagates to a larger L-shell and lower latitude, (2) a strong standing-wave pattern is formed in the LHR reflection region, and (3) the whistler emission turns from right-hand circularly polarized to linearly polarized near the reflection region. Finally, we run a simulation in which a quasi-electrostatic whistler is launched at a high latitude with a small-scale density irregularity added as a depletion to the background plasma. We find that a small portion of quasi-electrostatic whistler energy can be coupled to a parallel whistler, which can propagate to a much lower altitude while most of the wave energy experiences LHR reflection. Moreover, the mode coupling depends on the transverse and longitudinal sizes of the density irregularity. This makes a possible explanation of ground observations of nonducted whistler emission, which could have been reflected in the high-latitude ionosphere and magnetosphere.

## 1. Introduction

Whistler mode emissions in the extremely low frequency and very low frequency range in the magnetosphere have been investigated extensively because of their significant roles in the wave-particle interaction with energetic particles in the radiation belts (Helliwell, 1988; Kennel & Petschek, 1966; Xiao et al., 2017). The propagation characteristics of whistler mode emissions in the magnetosphere include refraction, reflection, guiding and scattering due to the variation of plasma density and geomagnetic field (He et al., 2015). These are also of vital importance, since they influence the spatial distribution and wave properties of the whistler emissions and subsequent interaction with particles (Sonwalkar, 2006).

For nonducted whistler emission, the wave normal angle increases during the propagation from the equator to high latitude. Likewise, the local lower hybrid resonance (LHR) frequency also increases. When the wave frequency becomes lower than the local LHR frequency, whistler waves rapidly turn wave normal perpendicular to the field line and thus can experience reflection toward the equator (Chum & Santolik, 2005; Jirícek et al., 2001; Lyons & Thorne, 1970; Shklyar et al., 2004). The LHR reflection (also known as magnetospheric reflection) in the magnetosphere has been predicted by the ray tracing method. It has been theoretically shown that ion effects are crucial to the LHR reflection and that the gradient of the geomagnetic strength along the field line contributes the most to the curvature of the whistler propagation path (Kimura, 1966; Lyons & Thorne, 1970). Meanwhile, several recent satellite observations of reflected chorus in the magnetosphere provide evidence for the theory of the LHR reflection (Agapitov et al., 2011; Breuillard et al., 2013; Parrot et al., 2004). Whistler emissions after LHR reflection are usually trapped in the magnetosphere, with some contributing to plasmaspheric hiss (Bortnik et al., 2008) and some evolving into LHR noise with a sharp lower cutoff at the LHR frequency (Brice & Smith, 1965; Burtis, 1973;

Jirícek et al., 2001; Shklyar et al., 2004). Although the LHR reflection has been predicted by the ray tracing method and some observations on the magnetospherically reflected whistler mode waves have been reported, the focus of these studies is usually on the low-latitude magnetosphere where in situ measurements of reflected waves are made. The detailed wave properties and energy distribution in the LHR reflection region at high latitude, therefore, are still yet to be investigated.

Ground observational studies reveal that magnetospheric whistler mode emission can reach the ground. A mechanism of ducted propagation, as opposed to nonducted propagation in a smooth media, is proposed to account for it reaching the ground without experiencing magnetospheric reflection (Helliwell, 1965). A magnetospheric density structure with a large transverse gradient along the field line from the equatorial magnetosphere to the ionosphere can change the wave normal angles of the whistler emissions and serve as a waveguide to trap and guide the whistler waves out of the magnetosphere and toward the ground (Inan & Bell, 1977; Woodroffe & Streltsov, 2013). However, such density irregularities with a large spatial scale along an entire field line have not yet been verified by direct observational evidence or physical justification, according to our best knowledge. Bell and Ngo (1990) propose that a quasi-electrostatic whistler mode, which is also a type of lower hybrid wave, can be excited by the interaction of a quasi-parallel whistler with a density irregularity at a spatial scale comparable to the perpendicular wavelength of the quasi-electrostatic whistler mode. This mode-coupling mechanism has been proved reversible by numerical simulation of linear mode conversion from a lower hybrid wave to a whistler under a low-altitude ionospheric plasma condition (Camporeale et al., 2012; Eliasson & Papadopoulos, 2008). However, most of these studies are confined to a uniform geomagnetic field, and therefore, the effect of LHR reflection is not considered. It is intriguing to investigate whether the presence of such localized small-scale density irregularities can significantly affect the propagation of whistlers with large wave normal angles near the LHR frequency and scatter them into quasi-parallel whistlers. If so, this would provide a possible mechanism for a nonducted magnetospheric whistler to avoid LHR reflection and reach the ground.

In our study, we first use a two-dimensional full-wave model to investigate the LHR reflection of nonducted whistler mode waves in a dipole field and the roles of proton response during the reflection. Detailed wave properties of the LHR reflection are studied, such as the wave structure and polarization, which may provide more information for future study on the magnetospheric reflection region. We also investigate the effects of small-scale density irregularities on the propagation of nonducted whistlers near the LHR frequency to see if the quasi-electrostatic whistler may be scattered to a quasi-parallel whistler and avoid LHR reflection. This could be a potential mechanism for magnetospheric whistlers to reach the ground. This paper is organized as follows: The full-wave model is introduced in section 2, the simulation results are presented in section 3, and section 4 comprises the conclusion and discussion.

## 2. Full-Wave Model

### 2.1. Basic Equations

The full-wave model is based on cold plasma theory (Helliwell, 1965; Stix, 1992), and the whistler mode wave propagation is studied by numerically solving the following electromagnetic wave equations:

$$\nabla \times \mathbf{E} = -\mu_0 \frac{\partial \mathbf{H}}{\partial t} \tag{1}$$

$$\nabla \times \mathbf{H} = \varepsilon_0 \frac{\partial \mathbf{E}}{\partial t} + \sum_\alpha \mathbf{J}_\alpha \tag{2}$$

$$\frac{\partial \mathbf{J}_\alpha}{\partial t} + \nu_\alpha \mathbf{J}_\alpha = \varepsilon_0 \omega_{p\alpha}^2 \mathbf{E} - \boldsymbol{\omega}_{c\alpha} \times \mathbf{J}_\alpha \tag{3}$$

Equations 1 and 2 are Maxwell equations, and equation 3 is the linearized momentum equation for cold plasma species (electron and proton in our case) denoted by $\alpha$. $\mathbf{E}$ and $\mathbf{H}$ are the electric and magnetic fields, respectively, and $\mathbf{J}_\alpha$ is the plasma current due to the $\alpha$ species. $\omega_{p\alpha}$ and $\boldsymbol{\omega}_{c\alpha}$ are the plasma frequency and

gyrofrequency for the $\alpha$ species, respectively, and $\nu_\alpha$ is the collision frequency for the $\alpha$ species. $\mu_0$ and $\varepsilon_0$ are the vacuum permeability and permittivity respectively.

### 2.2. Coordinate System

This set of equations are solved in a modified dipole coordinate system ($\psi$,$\nu$,$\phi$) (Kageyama et al., 2006) defined by spherical coordinates ($r$,$\theta$,$\phi$) with

$$\psi = \frac{sinh^{-1}\left(\frac{a\cos\theta}{r^2}\right)}{sinh^{-1}a} \tag{4}$$

$$\nu = \frac{\sin^2\theta}{r} \tag{5}$$

The $\psi$ axis is along the ambient magnetic field, the $\nu$ axis is perpendicular to the $\psi$ axis in the meridian plane, the $\phi$ axis is along the azimuthal direction and the parameter $a$ in equation 4 is used to adjust the spatial grid of the $\psi$ axis in the simulation region. In a standard dipole coordinate, the realistic grid spacing in the simulation region changes rapidly from the equator to high latitude, which makes the numerical stability condition unnecessarily severe. In this modified dipole coordinate, the variation of the spatial grid becomes slow with the proper setting of parameter $a$ (~100), which is suitable in our simulation. The simulation system is two-dimensional in our study, and whistler wave propagation along the $\psi$ and $\nu$ axis in meridian plane is considered.

### 2.3. Numerical Technique

Finite difference time domain method is adopted to solve Maxwell's equations (Liu et al., 2018; Taflove & Hagness, 2005) to update the **E** and **H** fields. The linearized momentum equation for the $\alpha$ species is solved to update the $\mathbf{J}_\alpha$ field using a modified Boris method (applicable in both collisional and collisionless regimes) following Samimi and Simpson (2015). The electric field **E** and plasma current field $\mathbf{J}_\alpha$ are collocated at the edges of each computational grid cell, while the magnetic field **H** is located at the centers of the cell in our case. $\mathbf{J}_\alpha$ and **H** field are advanced at half-integer time steps while the **E** field is advanced at integer time steps.

### 2.4. Boundary Condition

In our two-dimensional simulation domain of the grid cell numbers $N_\nu$ and $N_\psi$ in the $\nu$ and $\psi$ axis respectively, the collision frequency $\nu_\alpha$ is set to 0 in the inner simulation domain at least 100 grid points inward each of the four boundaries in the $\nu$ and $\psi$ axes and is enhanced quadratically inside the boundary layer (from the 100th grid points to the cells at the boundaries), thus creating an absorbing condition for the simulation system (Streltsov et al., 2006). The wave energy in the boundary layer quickly dissipates, so no significant wave energy can reflect back into the simulation region.

## 3. Simulation Results

The simulation study is set up to investigate the propagation of whistler emission near the local LHR frequency in a realistic ambient magnetic field and plasma density. A magnetic dipole field

$$\boldsymbol{B}_0 = \frac{\nabla\psi}{|\nabla\psi|} B_{eq}\left(\frac{1}{L\cos^2\theta}\right)^3 \sqrt{1+3\sin^2\theta} \tag{6}$$

is adopted as the ambient magnetic field, where $\frac{\nabla\psi}{|\nabla\psi|}$ is a unit vector along the $\psi$ axis, $B_{eq}$ is the equatorial magnetic field strength, $L$ is the L-shell value, and $\theta$ is the magnetic latitude. The plasma density profile is adjusted accordingly to simulate whistler propagation in the magnetosphere. In our simulation system, the wave frequency is normalized to the local electron gyrofrequency and the dipole field strength and plasma density are scaled to smaller values while keeping the ratio $\frac{\omega_{p\alpha}^2}{\omega_{c\alpha}^2}$ constant. By doing so, the wave frequency is less and the wavelength used in the simulation system is longer than that in the original plasma medium. With lower wave frequency and longer wavelength, it takes fewer time steps and less computation grids in the simulation for whistler propagation in the dipole field. A spatially Gaussian wave source along the $\nu$ axis is set up at the lower $\psi$ boundary (corresponding to the lower latitude boundary). The $H_\phi$

component of the linear source oscillates sinusoidally at frequency $f$ with a certain initial wave normal angle, following the form of

$$H_\phi(\nu, t) = \sin\left(\int k_\nu h_\nu \mathrm{d}\nu + 2\pi f t\right)\exp\left(-\frac{(L-L_0)^2}{D_{L0}^2}\right) \tag{7}$$

$k_\nu$ is the perpendicular wave number, which is obtained from the cold plasma dispersion of the whistler mode for the given values of the wave normal angle and $f$ at the center of the line source. This ensures that the source wave propagates at the chosen wave normal angle. $h_\nu = \frac{1}{|\nabla\nu|}$ is the metric term defined in the coordinate system. $L_0$ and $D_{L0}$ are the center and half width of the Gaussian shaped wave source, respectively.

### 3.1. Propagation of Whistler Emission in a Dipole Field With Uniform Plasma Density

First, we simulate the propagation of whistler emission in a dipole field with a uniform plasma density. The simulation is performed in a $N_\nu \times N_\psi$ grid with $N_\nu = 500$ and $N_\psi = 901$, and the time step is $\Delta t = 5.0 \times 10^{-7}$ s. The original $B_{eq}$ is $3.12 \times 10^{-5}$ T, and the plasma density is $1.0 \times 10^7$ m$^{-3}$. After normalization, $B_{eq}$ is scaled down to $3.12 \times 10^{-6}$ T, the plasma density is $1.0 \times 10^5$ m$^{-3}$ and the oscillating frequency of the wave source is 40 Hz, with the ratio of wave frequency to the local electron gyrofrequency in the source region $\left(\frac{\omega}{\omega_{ce}}\right)_{source} = 0.042$ and the ratio of the wave frequency to the local $f_{LHR}$ in the source region $\left(\frac{f}{f_{LHR}}\right)_{source} = 1.90$. The center of the wave source is at $L_0 = 4.5$ in the equatorial region. The half width $D_{L0}$ is 0.0111, and the initial wave normal angle is 0°. The L-shell range of the simulation system is from 4.0 to 5.5, and the magnetic latitude range is from 0° to 40°. The spatial profile of the local LHR frequency $f_{LHR}$ and the ratio of the electron plasma frequency to gyrofrequency $\frac{\omega_{pe}}{\omega_{ce}}$ calculated with the scaled plasma parameters in the simulation system are shown in Figure 1.

The simulation is run under two different plasma conditions: electron plasma (with assumed stationary protons) and plasma including electrons and protons. The simulation is run over 40 wave periods in both cases. The simulation results are presented in Figures 2 and 3. Figure 2 shows the electromagnetic components of the whistler emission in both cases. During the simulation, we sample the signal in each grid cell of the simulation system in the time domain. With these sampling signals, we calculate the following wave properties: (1) Time-averaged Poynting vector calculated with

$$\boldsymbol{S} = \frac{1}{T}\int \mathbf{E} \times \mathbf{H} \mathrm{d}t \tag{8}$$

where $T$ is the whistler wave period; (2) polar angle of the Poynting vector calculated using the components of $\boldsymbol{S}$; and (3) wave normal angle and ellipticity of the magnetic field polarization calculated by the Means method (Means, 1972). The wave properties (Poynting flux magnitude and direction, ellipticity, and wave normal angles) for both cases are demonstrated in Figure 3.

For the initialization of the wave simulation, the whistler emission is assigned a parallel propagation in the line source region, and the wave frequency is above the local LHR frequency. As shown in Figures 2c–2f, the wave front of the whistler emission is perpendicular to the dipole field line near the equator, the wave normal angle is nearly 0° (Figures 3g and 3h) and the ellipticity is nearly 1 (Figures 3e and 3f), which indicates a right-handed circular polarization. As the whistler emission propagates away from the equator, the wave front is tilted toward a higher L-shell (Figures 2c–2f) due to the ambient magnetic field curvature. The wave normal angle is increasing, while the whistler emission is still propagating toward a higher latitude along the dipole field line, as indicated by the polar angle of the Poynting vector being near zero (Figures 3c and 3d). When the whistler emission propagates to where the wave frequency is close to the local LHR frequency of 40 Hz, and the ratio of the electron plasma frequency to the gyrofrequency is around unity, the wave front becomes nearly parallel to the dipole field line (Figures 2a, 2b, 2e, and 2f) and the wave normal angle becomes close to 90° (Figures 3g and 3h). During the propagation away from the equator, the $E_\nu$ component amplitude increases from a small but finite value ~0.5 near the equator to an order of magnitude higher at high latitude (Figures 2a and 2b), while the $B_\nu$ component weakens (Figures 2c and 2d), indicating that the whistler emission becomes quasi-electrostatic. In the case of electron plasma, the quasi-electrostatic whistler

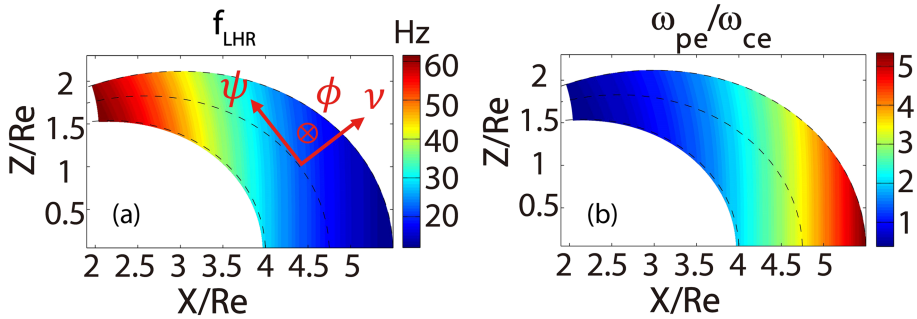


**Figure 1.** (a) Local LHR frequency $f_{LHR}$ with scaled plasma parameters. (b) Ratio of electron plasma frequency to gyrofrequency $\frac{\omega_{pe}}{\omega_{ce}}$ . The dashed curves in each panel represent the dipole field lines. The $\psi$, $\nu$, and $\phi$ axis of the simulation system are shown in (a).

emission keeps propagating to a higher latitude until being absorbed in the upper latitude boundary. When proton motion is added to the plasma current response, the whistler emission rapidly changes from right-handed polarization to linear polarization and reflects back to a higher L-shell and lower latitude. The reflected whistler emission is propagating along the dipole field line (Figure 3d), but with an oblique wave normal angle of 110° (Figure 3h). The simulation of the whistler reflection in plasma including electrons and protons is similar to the magnetospheric reflection, and it is consistent with ray tracing calculations (Bortnik et al., 2008; Bortnik et al., 2011; He et al., 2015; Kimura, 1966; Lyons & Thorne, 1970).

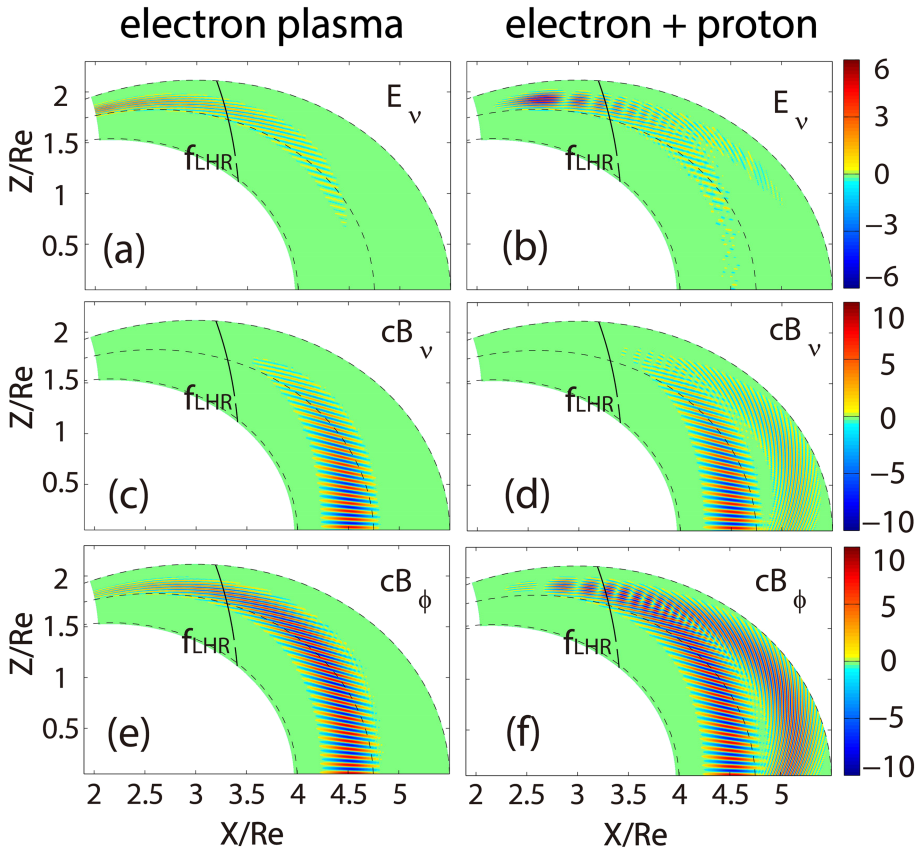


**Figure 2.** Whistler electromagnetic field components in a dipole field with uniform density profile. (a) and (b) show the $E_\nu$ component, (c) and (d) show the $B_\nu$ component times the light speed $c$, and (e) and (f) show the $B_\phi$ component times the light speed $c$. Panels (a), (c), and (e) are from the whistler propagation simulation of electron plasma, and panels (b), (d) and (f) are from the simulation of plasma including both electrons and protons. The contours in each panel denote where wave the frequency matches the local LHR frequency $f_{LHR}$.

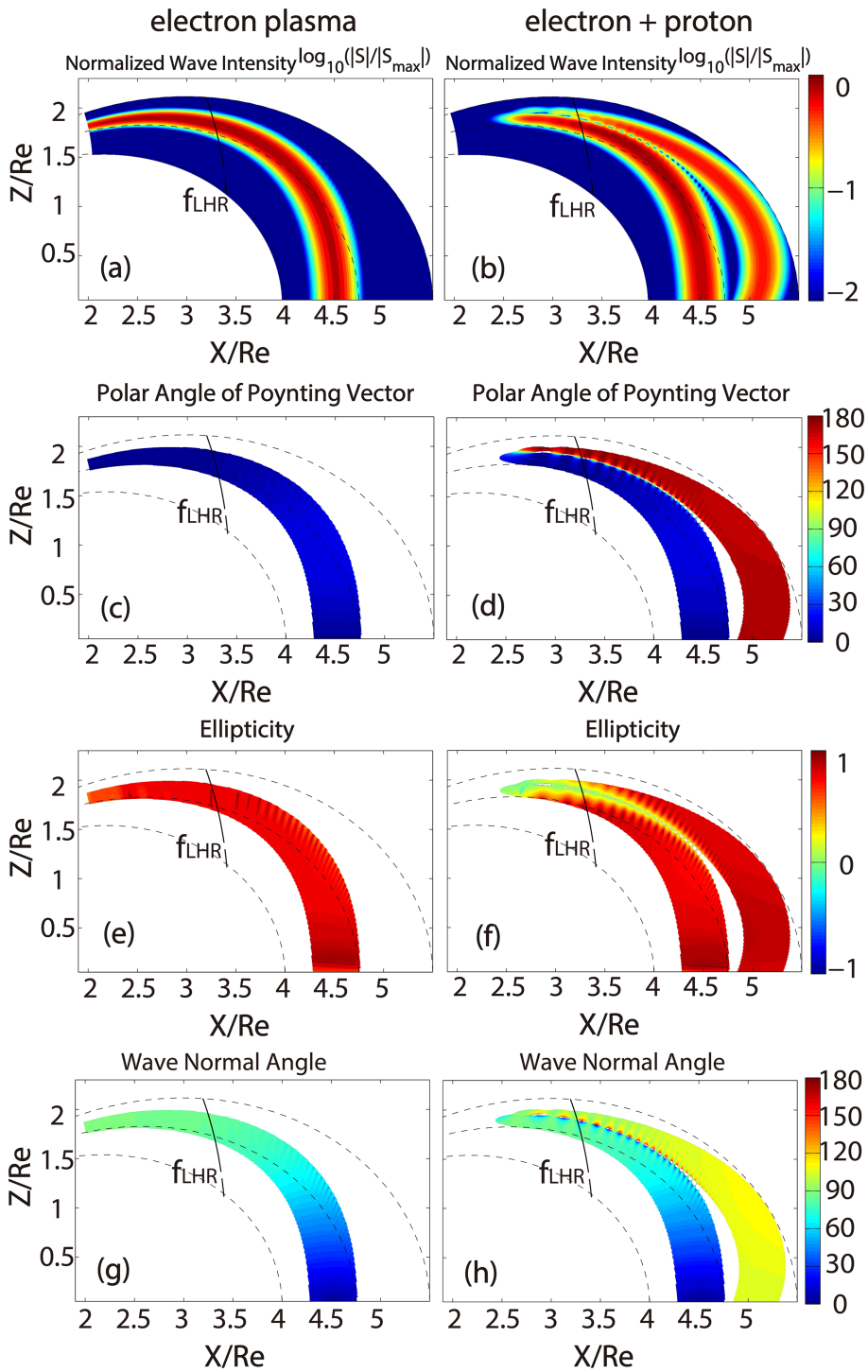


**Figure 3.** (a) and (b) are the normalized wave intensity $log_{10}\left(\frac{|\boldsymbol{S}|}{|\boldsymbol{S}_{max}|}\right)$. (c) and (d) are the polar angle of the Poynting vector $\boldsymbol{S}$ with respect to the ambient magnetic field. "0" represents the wave energy propagating parallel to the ambient magnetic field, and "180" represents the antiparallel situation. (e) and (f) are the wave normal angle with respect to the ambient magnetic field. "0" denotes the wave normal parallel to the ambient magnetic field, and "180" is for the antiparallel situation. (g) and (h) are the ellipticity of the magnetic field polarization. "1" is for a purely right-hand circular polarization, "0" is for a linear polarization, and "−1" is for a purely left-hand circular polarization. Panels (a), (c), (e), and (g) are from the whistler propagation simulation of electron plasma, and panels (b), (d), (f), and (h) are from the simulation of plasma including both electrons and protons.

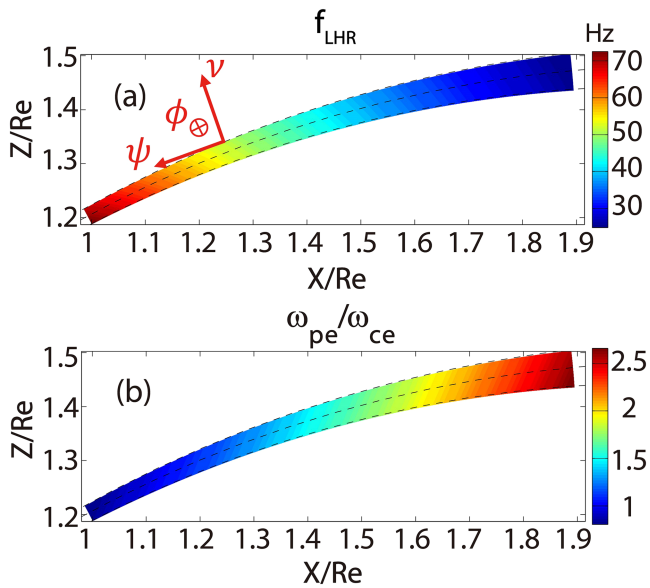


**Figure 4.** (a) Local LHR frequency $f_{LHR}$ with scaled plasma parameters. (b) Ratio of electron plasma frequency to gyrofrequency $\frac{\omega_{pe}}{\omega_{ce}}$. The dashed curves in each panel represent the dipole field lines. The $\psi$, $\nu$, and $\phi$ axis of the simulation system are shown in (a).

A pronounced standing wave is formed near the reflection region extending a range of latitudes, due to the interference of the whistler waves propagating in opposite directions (Figures 2b and 2f). Such an interference pattern may be of great value to verify magnetospheric reflection and identify the reflection region from the observation. It should also be noted that the whistler emission is mostly right-handed polarized except for the reflection and interference region where linear polarization is shown (Figure 3h). The whistler mode wave cannot access an altitude below the magnetospheric reflection, not to mention the ground. In other words, the magnetospheric reflection is a virtual barrier preventing the emission from reaching the ground and reaching the ground requires additional physical processes.

### 3.2. Propagation of Whistler Emission Near the Local LHR Frequency With Small-Scale Density Irregularity

As illustrated in section 3.1, the whistler emission becomes quasi-electrostatic and the wave normal angle becomes close to 90° where the wave frequency is close to the local LHR frequency. This kind of whistler emission can be identified as a lower hybrid wave (Helliwell, 1965). and it can be coupled to a quasi-parallel propagating whistler emission with the presence of small-scale density irregularities (Bell & Ngo, 1990; Camporeale et al., 2012; Eliasson & Papadopoulos, 2008). This section investigates the effects of the density irregularity on the propagation of whistler emission near the local LHR frequency.

The simulation is performed with $N_\nu = 800$ and $N_\psi = 901$, and the time step is $\Delta t = 5.0 \times 10^{-7}$ s. The original $B_{eq}$ is $3.12 \times 10^{-5}$ T, and the plasma density is adopted from a diffusive equilibrium plasma density model with the same parameters used in Bortnik et al. (2011). After normalization, the $B_{eq}$ is scaled down to $3.9 \times 10^{-7}$ T, the plasma density is obtained by keeping the ratio $\frac{\omega_{p\alpha}^2}{\omega_{c\alpha}^2}$ constant, and the oscillating frequency of the wave source is 50 Hz, with the ratio of the wave frequency to the local electron gyrofrequency in the source region $\left(\frac{\omega}{\omega_{ce}}\right)_{source} = 0.043$ and the ratio of the wave frequency to the local $f_{LHR}$ in the source region $\left(\frac{f}{f_{LHR}}\right)_{source} = 1.99$ at high latitude. The center of the wave source is set at $L_0 = 3.87$ (near the middle dipole field line in Figures 4 and 5), the latitude of 38.8° and the geocentric distance of 2.35 $R_e$. The half width $D_{L0}$ is 0.0063, and the initial wave normal angle is 87.62°. With such an oblique initial wave normal angle and wave frequency just above the LHR frequency in the source, the wave, if not ducted, would experience magnetospheric reflection soon. The L-shell range of the simulation system is from 3.74 to 3.94, the magnetic latitude range is from 38° to 51° and the geocentric distance range is from 1.56 $R_e$ to 2.35 $R_e$. The spatial profile of the local LHR frequency $f_{LHR}$ and the ratio of electron plasma frequency to gyrofrequency $\frac{\omega_{pe}}{\omega_{ce}}$ calculated with scaled plasma parameters without the presence of density irregularity in the simulation system are shown in Figure 4. Two cases are simulated in this section: with and without the density irregularity. Small-scale localized density irregularities have been observed by the Freja satellite in the ionosphere (Høymork et al., 2001) and by the Viking and Cluster satellites in the inner magnetosphere (Tjulin et al., 2003). These irregularities are generally considered to be lower hybrid density cavity depletion due to transverse ion acceleration (Knudsen et al., 2004; Vago et al., 1992) and have a Gaussian shape across the ambient magnetic field (Høymork et al., 2001). So in this section, the

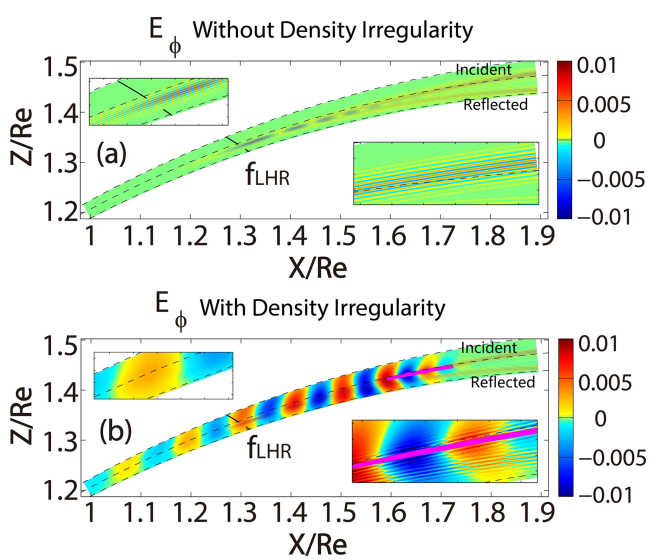


**Figure 5.** Azimuthal component of the whistler electric field $E_\phi$ near the local LHR frequency at high latitude. (a) $E_\phi$ component without a density irregularity. (b) $E_\phi$ component with a density irregularity. Contours in each panel denote where the wave frequency matches the local LHR frequency $f_{LHR}$. The magenta bold line denotes the shape and location of the density irregularity in (b).

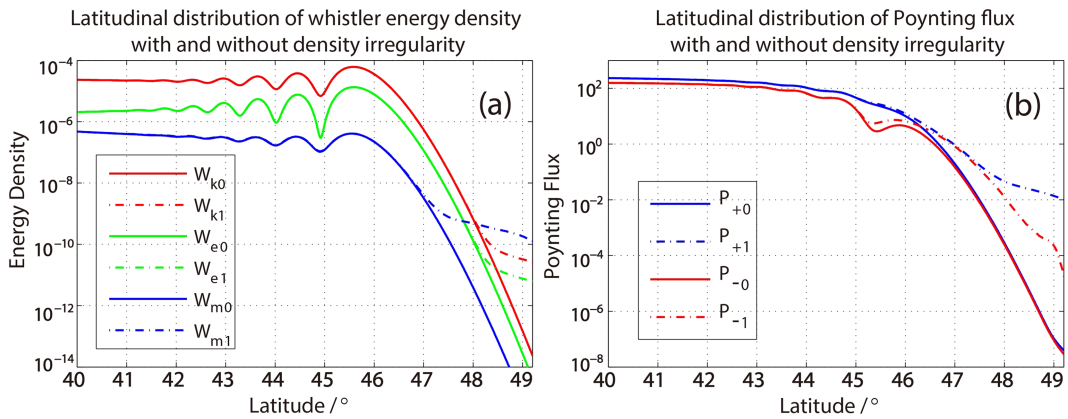


**Figure 6.** (a) Latitudinal distribution of the whistler energy density with and without the density irregularity. (b) Latitudinal distribution of the Poynting flux with and without the density irregularity. In panel (a), the red, green, and blue solid lines show the kinetic energy density $W_{k0}$, the electric energy density $W_{e0}$, and the magnetic energy density $W_{m0}$ without the density irregularity, respectively. The dash-dotted lines represent the corresponding energy density ($W_{k1}$, $W_{e1}$, and $W_{m1}$) with the presence of the density irregularity. In panel (b), the blue and red solid lines show the magnitude of the positive Poynting flux $P_{+0}$ (pointing toward higher latitude) and the negative Poynting flux $P_{-0}$ (pointing toward lower latitude) without the density irregularity, respectively. The dash-dotted lines represent the corresponding Poynting flux ($P_{+1}$ and $P_{-1}$) with the presence of the density irregularity.

density irregularity over a spatially localized region is added as a depletion to the background plasma density and is given by

$$N_d = \delta N \exp\left(-\left(\frac{L-L_d}{D_L}\right)^2 - \left(\frac{r-r_d}{D_r}\right)^2\right) \tag{9}$$

where $\delta N$ is the center density depletion percentage relative to the background plasma density and $L_d$ and $D_L$, respectively, are the L-shell and transverse size of the density depletion (half-width of the Gaussian shaped density depletion in the direction perpendicular to the dipole field). $r_d$ and $D_r$, respectively, are the geocentric distance and longitudinal size of the density depletion (half-width of the Gaussian shaped density depletion in the direction parallel to the dipole field). In our simulation, the nominal parameters for the density irregularity are set as the following unless explicitly mentioned otherwise; $\delta N$ is set to be 10%, $L_d$ is 3.84, $D_L$ is 0.0021, $r_d$ is 2.19 $R_e$, and $D_r$ is 0.063 $R_e$. The simulation is run over 100 wave periods in both cases.

Simulation results of the $E_\phi$ component are shown in Figure 5. As shown in Figures 5a and 5b the wave front of the quasi-electrostatic whistler emission is almost parallel to the dipole field line at high latitude, and the incident wave energy propagates mainly along the dipole field line. The incident whistler emission reflects backward from the region where the wave frequency is below the local LHR frequency. Contrary to the case in section 3.1, the reflected wave propagates to a lower L-shell. Also, a strong standing wave is formed near the reflection region. When the small-scale density depletion irregularity is added to the simulation region, significant parallel whistler emission arises near the density irregularity, and the amplitude of the $E_\phi$ component is enhanced (Figure 5b) compared to the case without the irregularity (Figure 5a). This can be explained by the linear mode coupling theory as in Bell and Ngo (1990). Despite the limited parallel spatial size of the density irregularity, the stimulated parallel whistler can propagate along the dipole field line to lower altitude than the reflection region without significant change of the wave normal angle.

During the simulation, signals in each computational cell are sampled in the time domain as in section 3.1. In order to investigate the latitudinal distribution of the whistler energy density in the simulation region, we calculate the spatial integral of the time-averaged magnetic, electric and kinetic energy density along the $\nu$ axis (perpendicular to the magnetic field line direction), respectively, using the following equations:

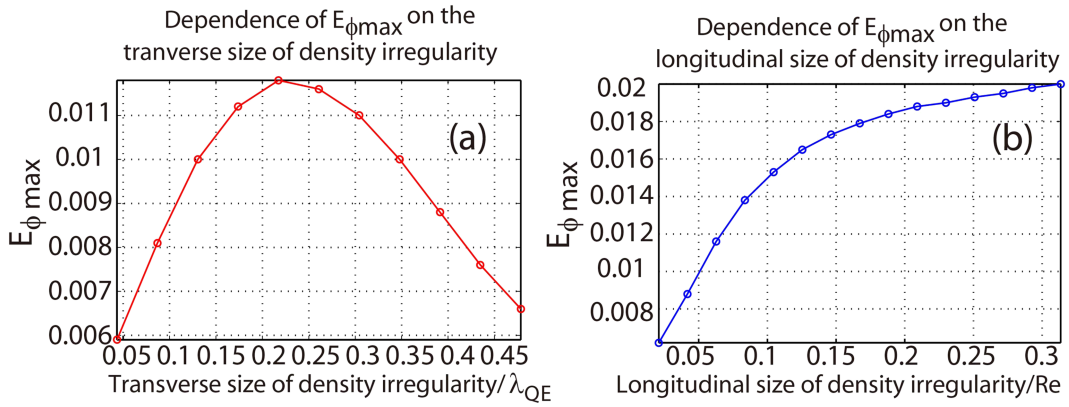


**Figure 7.** (a) Dependence of $E_{\phi max}$ on the transverse size of the density irregularity. The horizontal axis is the transverse size normalized to the perpendicular wavelength $\lambda_{QE}$ of the quasi-electrostatic whistler near the mode conversion region. (b) Dependence of $E_{\phi max}$ on the longitudinal size of the density irregularity. The horizontal axis is the longitudinal size normalized to $R_e$.

$$W_m = \int \frac{1}{T} \int \frac{1}{2} \mu_0 \left( H_\psi^2 + H_\nu^2 + H_\phi^2 \right) \mathrm{d}t h_\nu \mathrm{d}\nu \tag{10}$$

$$W_e = \int \frac{1}{T} \int \frac{1}{2} \varepsilon_0 \left( E_\psi^2 + E_\nu^2 + E_\phi^2 \right) \mathrm{d}t h_\nu \mathrm{d}\nu \tag{11}$$

$$W_k = \int \frac{1}{T} \int \sum_\alpha \frac{m_\alpha}{2e^2 N_\alpha} \left( J_\psi^2 + J_\nu^2 + J_\phi^2 \right) \mathrm{d}t h_\nu \mathrm{d}\nu \tag{12}$$

where $T$ is the whistler wave period, $m_\alpha$ is the mass of electron or proton, $N_\alpha$ is the plasma density, and $e$ is the elementary charge.

To obtain the latitudinal distribution of the whistler Poynting flux in the simulation region, we define the positive (negative) time-averaged Poynting vector $\boldsymbol{S}_+(\boldsymbol{S}_-)$ with the criterion $\boldsymbol{S} \cdot \boldsymbol{B}_0 > 0(<0)$ and calculate the positive Poynting flux $P_+$ (pointing to higher latitude) and the negative Poynting flux $P_-$ (pointing to lower latitude) using the following equations:

$$P_\pm = \int |\boldsymbol{S}_\pm| h_\nu \mathrm{d}\nu \tag{13}$$

The latitudinal distribution of the whistler energy density and the Poynting flux are shown in Figures 6a and 6b, respectively. The solid lines show the case without the density irregularity and are denoted with the subscript "0." The dash-dotted lines show the case with the density irregularity and are denoted with the subscript "1." Without the density irregularity, electric and kinetic energy dominate in the whole simulation region, which shows the electrostatic characteristic nature of the highly oblique whistler emission. The whistler energy density shows an oscillatory pattern below the latitude of 46° with several peaks and valleys (Figure 6a), as signatures of the standing wave structure due to the magnetospheric reflection. Both the positive and negative Poynting fluxes in Figure 6b drop rapidly with almost the same rate above the latitude of 46°. That is, no significant wave energy propagates across the magnetospheric reflection region. The energy density in Figure 6a shows the same feature above the latitude of 46° after maximizing between the latitude of 45° and 46°.

When a localized density irregularity is added below the reflection region, both the whistler energy density (Figure 6a) and the Poynting flux (Figure 6b) show a similar pattern to the case without the density irregularity below the latitude of 46°. However, above the latitude of 47°, the positive Poynting flux becomes larger than the negative Poynting flux $P_{-1}$ and decreases much slower than the negative Poynting flux (Figure 6b), which shows that a certain amount of wave energy can transmit through the magnetospheric reflection region and propagate toward a higher latitude. Unlike the obliquely propagating whistler at lower latitude (<46°), the transmitted wave carries the magnetic energy density much larger than the electric and

kinetic density by an order of magnitude (Figure 6a), indicating the transmitted wave propagates in the quasi-parallel direction.

Finally, we investigate the effect of spatial size of localized density irregularities on the efficiency of this linear mode conversion from quasi-electrostatic whistler waves to parallel propagating whistler waves in a dipole field. We run the above simulation with density irregularity of different transverse size $D_L$ and longitudinal size $D_r$. The maximum of azimuthal electric component $E_{\phi max}$ is used to denote the efficiency of this linear mode conversion since, as shown in Figure 5, the significant enhancement of the $E_\phi$ component is associated with the conversion to parallel whistler waves. The dependence of $E_{\phi max}$ on the transverse size and longitudinal size of density irregularities is shown in Figures 7a and 7b respectively. The perpendicular wavelength $\lambda_{QE}$ of the quasi-electrostatic whistler wave near the mode conversion region is about 0.0079 in $L$ value, and the transverse size $D_L$ is normalized to $\lambda_{QE}$ in Figure 7a. As shown in Figure 7a, the $E_{\phi max}$ value has a peak when transverse size $D_L$ is about $0.22\lambda_{QE}$. In other words, the mode conversion efficiency maximizes when the ratio of the transverse size of density irregularity to the perpendicular wavelength of the quasi-electrostatic whistler is about 0.22. This is consistent with the conclusion in Eliasson and Papadopoulos (2008) and Camporeale et al. (2012). As for the dependence on the longitudinal size, the mode conversion efficiency increases linearly with the longitudinal size of the density irregularity when the longitudinal size is smaller than 0.1 $R_e$ as shown in Figure 7b. This increasing of the efficiency gradually slows down when the longitudinal size becomes larger than 0.1 $R_e$.

## 4. Conclusions and Discussion

Propagation of whistler emission near the local LHR frequency in a magnetic dipole field is investigated using a two-dimensional full-wave model. First, we study the propagation of parallel whistler emission launched from an equatorial region where the wave frequency is above the local LHR frequency with uniform plasma density profile in electron plasma. Then we make comparison with simulation results with the proton current response added. Finally, the propagation of whistler waves near the local LHR frequency at high latitude with small-scale density irregularity over a localized region is simulated. Principal conclusions are drawn as follows:

1. The 2-D full-wave simulation verifies the existence of magnetospheric reflection of a nonducted whistler wave predicted by ray tracing when the proton response is considered. In electron plasma, the quasi-electrostatic whistler transforms from parallel whistler emission due to the ambient magnetic curvature and continues to propagate until being absorbed in upper latitude boundary. With proton current added, the quasi-electrostatic whistler reflects from where the wave frequency is below the local LHR frequency to a lower latitude with a rather oblique wave normal angle.
2. The full-wave simulation shows that the magnetospheric reflection is accompanied with a pronounced standing wave structure, which may be of great value as a signature for identifying the magnetospheric reflection region. In such a standing wave structure in the reflection region, the wave polarization changes from right-handed circular to nearly linear.
3. The 2-D full-wave simulation shows the whistler wave energy cannot reach a low altitude, not to mention the ground, without additional physical processes because of magnetospheric reflections.
4. To account for whistler mode waves reaching the ground from the magnetosphere, we propose the linear mode conversion of electrostatic lower hybrid waves to parallel propagating whistler waves by a localized density irregularity near the magnetospheric reflection. Such a proposed mechanism does not require a density structure with a transverse gradient throughout an entire field line, as required by ducting propagation.
5. The efficiency of the linear mode conversion depends on both the transverse size and longitudinal size of the localized density irregularities. The efficiency maximizes when the ratio of the transverse size to the perpendicular wavelength of quasi-electrostatic whistler is about 0.22. The efficiency increases linearly with the longitudinal size when the size is small, and this increase gradually slows down for larger size.

In section 3.1, a uniform plasma density profile is adopted instead of a diffusive equilibrium plasma density model (Bortnik et al., 2011). Nevertheless, the propagation path of the whistler emission in our simulation is consistent with the ray tracing results of the LHR reflection in the magnetosphere (Bortnik et al., 2011, 2008; He et al., 2015; Kimura, 1966; Lyons & Thorne, 1970). This shows that the ambient magnetic field gradient

and curvature play much more important roles than the plasma density in the magnetospheric LHR reflection (Lyons & Thorne, 1970).

In section 3.2, we use a small-scale density irregularity with a 10% density depletion. Although the density depletion is usually taken to be 5% (Bell & Ngo, 1990; Eliasson & Papadopoulos, 2008), we can still expect a stimulated parallel whistler with half of the energy if we drop the density depletion to 5% in our present simulation, since this is a linear process. Sonwalkar and Harikumar (2000) propose that auroral hiss from a few kHz to 10 kHz at high altitude (5,000–20,000 km) with a large wave normal angle can be scattered by a small-scale density irregularity to a whistler with a small wave normal angle, thus propagating to a much lower altitude and even penetrate to the ground. Moreover, only 0.1% to 10% of the scattered whistler emission has a small wave normal angle, and most of the auroral hiss energy experiences LHR reflection and stays at high altitude. This is consistent with the low conversion efficiency obtained in our simulation in section 3.2. Bell et al. (2004) report that a strong lower hybrid wave can be excited through linear mode coupling with a whistler at altitudes above 20,000 km, which suggests the existence of a small-scale density irregularity in the inner magnetosphere. This provides the evidence that the simulation results in section 3.2 may be applicable to the inner magnetosphere.

It should be noted that whistler wave propagates toward higher L-shell after LHR reflection in the case of section 3.1 while propagates toward lower L-shell in the case of section 3.2. This indicates that the transverse propagation direction of the reflected whistler waves may depend on their initial wave properties, such as wave frequency and wave normal angle (Bortnik et al., 2008; Bortnik et al., 2011; He et al., 2015). It should also be mentioned that a strong standing wave pattern and linear polarization in the LHR reflection region, which are shown in our simulation results in sections 3.1 and 3.2, are similar to the observation in a laboratory plasma experiment on the new reflection mechanism of whistler mode waves by Stenzel and Urrutia (2017). The signatures from simulated magnetospheric reflection can be compared with observation evidence from satellites near the LHR reflection region in the magnetosphere, which is left as a future study.

**Acknowledgments**
The simulation data in this paper can be accessed via the following link (http://doi.org/10.5281/zenodo.3592232). No observational data are used. X. X. would like to acknowledge the support by China Scholarship Council during his visit to the University of Texas at Dallas. L. C. acknowledges the support of the AFOSR grant of FA9550-16-1-0344. C. Z. acknowledges the support of the National Natural Science Foundation of China (NSFC Grants 41574146 and 41774162), the National Key R&D Program of China (Grant 2018YFC1503506), the foundation of National Key Laboratory of Electromagnetic Environment (Grant 6142403180204), and by Excellent Youth Foundation of Hubei Provincial Natural Science Foundation (Grant 2019CFA054).

## References

Agapitov, O., Krasnoselskikh, V., Zaliznyak, Y., Angelopoulos, V., Le Contel, O., & Rolland, G. (2011). Observations and modeling of forward and reflected chorus waves captured by THEMIS. *Annales de Geophysique*, *29*, 541–550. https://doi.org/10.5194/angeo-29-541-2011

Bell, T. F., Inan, U. S., Platino, M., Pickett, J. S., Kossey, P. A., & Kennedy, E. J. (2004). CLUSTER observations of lower hybrid waves excited at high altitudes by electromagnetic whistler mode signals from the HAARP facility. *Geophysical Research Letters*, *31*, L06811. https://doi.org/10.1029/2003GL018855

Bell, T. F., & Ngo, H. D. (1990). Electrostatic lower hybrid waves excited by electromagnetic whistler mode waves scattering from planar magnetic field-aligned plasma density irregularities. *Journal of Geophysical Research*, *95*(A1), 149-172.

Bortnik, J., Chen, L., Li, W., Thorne, R. M., & Horne, R. B. (2011). Modeling the evolution of chorus waves into plasmaspheric hiss. *Journal of Geophysical Research*, *116*, A08221. https://doi.org/10.1029/2011JA016499

Bortnik, J., Thorne, R. M., & Meredith, N. P. (2008). The unexpected origin of plasmaspheric hiss from discrete chorus emissions. *Nature*, *452*(7183), 62–66. https://doi.org/10.1038/nature06741

Breuillard, H., Zaliznyak, Y., Agapitov, O., Artemyev, A., Krasnoselskikh, V., & Rolland, G. (2013). Spatial spreading of magnetospherically reflected chorus elements in the inner magnetosphere. *Annales de Geophysique*, *31*(8), 1429–1435. https://doi.org/10.5194/angeo-31-1429-2013

Brice, N. M., & Smith, R. L. (1965). Lower hybrid resonance emissions. *Journal of Geophysical Research*, *70*, 71–80.

Burtis, W. J. (1973). Electron concentrations calculated from the lower hybrid resonance noise band observed by OGO 3. *Journal of Geophysical Research*, *78*, 5515–5523.

Camporeale, E., Delzanno, G. L., & Colestock, P. (2012). Lower hybrid to whistler mode conversion on a density striation. *Journal of Geophysical Research*, *117*, A10315. https://doi.org/10.1029/2012JA017726

Chum, J., & Santolik, O. (2005). Propagation of whistler mode chorus to low altitudes: Divergent ray trajectories and ground accessibility. *Annales de Geophysique*, *23*, 3727–3738. https://doi.org/10.5194/angeo-23-3727-2005

Eliasson, B., & Papadopoulos, K. (2008). Numerical study of mode conversion between lower hybrid and whistler waves on short-scale density striations. *Journal of Geophysical Research*, *113*, A09315. https://doi.org/10.1029/2008JA013261

He, Y., Xiao, F., Zhou, Q., Yang, C., Liu, S., Baker, D. N., et al. (2015). Van Allen Probes observation and modeling of chorus excitation and propagation during weak geomagnetic activities. *Journal of Geophysical Research: Space Physics*, *120*, 6371–6385. https://doi.org/10.1002/2015JA021376

Helliwell, R. A. (1965). *Whistlers and related ionospheric phenomena*. Press, Stanford, Calif: Stanford Univ.

Helliwell, R. A. (1988). VLF wave simulation experiments in the magnetosphere from Siple Station, Antarctica. *Reviews of Geophysics*, *26*(3), 551.

Høymork, S. H., Pecseli, H. L., Lybekk, B., Trulsen, J., & Eriksson, A. (2001). The shape and evolution of lower hybrid density cavities observed by FREJA. *Physics and Chemistry of the Earth, Part C*, *26*(1–3), 213–217.

Inan, U. S., & Bell, T. F. (1977). The plasmapause as a VLF wave guide. *Journal of Geophysical Research*, *82*, 2819.

Jirícek, F., Shklyar, D. R., & Tríska, P. (2001). LHR effects in nonducted whistler propogation—New observations and numerical modelling. *Annales de Geophysique*, *19*, 147–157.

Kageyama, A., Sugiyama, T., Watanabe, K., & Sato, T. (2006). A note on the dipole coordinates. *Computational Geosciences*, *32*, 265–269. https://doi.org/10.1016/j.cageo.2005.06.006

Kennel, C. F., & Petschek, H. E. (1966). Limit on stably trapped particle fluxes. *Journal of Geophysical Research*, *71*(1), 1–28. https://doi.org/10.1029/JZ071i001p00001

Kimura, I. (1966). Effects of ions on whistler-mode ray tracing. *Radio Science*, *1*(3), 269–283.

Knudsen, D. J., Bock, B. J. J., Bounds, S. R., Burchill, J. K., Clemmons, J. H., Curtis, J. D., et al. (2004). Lower-hybrid cavity density depletions as a result of transverse ion acceleration localized on the gyroradius scale. *Journal of Geophysical Research*, *109*, A04212. https://doi.org/10.1029/2003JA010089

Liu, X., Chen, L., Yang, L., Xia, Z., & Malaspina, D. M. (2018). One-dimensional full wave simulation of equatorial magnetosonic wave propagation in an inhomogeneous magnetosphere. *Journal of Geophysical Research: Space Physics*, *123*, 587–599. https://doi.org/10.1002/2017JA024336

Lyons, L., & Thorne, R. (1970). The magnetospheric reflection of whistlers. *Planetary and Space Science*, *18*(12), 1753–1767. https://doi.org/10.1016/0032-0633(70)90009-7

Means, J. D. (1972). Use of the three-dimensional covariance matrix in analyzing the polarization properties of plane waves. *Journal of Geophysical Research*, *77*, 5551–5559.

Parrot, M., Santolík, O., Gurnett, D., Pickett, J., & Cornilleau Wehrlin, N. (2004). Characteristics of magnetospherically reflected chorus waves observed by Cluster. *Annales de Geophysique*, *22*, 2597–2606. https://doi.org/10.5194/angeo-22-2597-2004

Samimi, A., & Simpson, J. J. (2015). An efficient 3-D FDTD model of electromagnetic wave propagation in magnetized plasma. *IEEE Transactions on Antennas and Propagation*, *63*(1), 269–279. https://doi.org/10.1109/TAP.2014.2366203

Shklyar, D., Chum, J., & Jirícek, F. (2004). Characteristic properties of Nu whistlers as inferred from observations and numerical modelling. *Annales de Geophysique*, *22*, 3589–3606. https://doi.org/10.5194/angeo-22-3589-2004

Sonwalkar, V. S. (2006). The influence of plasma density irregularities on whistler mode wave propagation. In *Geospace electromagnetic waves and radiation* (pp. 191, 141–190). Berlin: Springer.

Sonwalkar, V. S., & Harikumar, J. (2000). An explanation of ground observations of auroral hiss: Role of density depletions and meter-scale irregularities. *Journal of Geophysical Research*, *105*(A8), 18,867–18,883.

Stenzel, R. L., & Urrutia, J. M. (2017). New properties of whistler modes. *Geophysical Research Letters*, *44*, 2113–2119. https://doi.org/10.1002/2016GL072446

Stix, T. H. (1992). *Waves in plasmas*. New York: AIP Press.

Streltsov, A. V., Lampe, M., Manheimer, W., Ganguli, G., & Joyce, G. (2006). Whistler propagation in an inhomogeneous plasma. *Journal of Geophysical Research*, *111*, A03216. https://doi.org/10.1029/2005JA011357

Taflove, A., & Hagness, S. C. (2005). *Computational electromagnetics: Finite-difference time-domain method*. Norwell, MA, USA: Artech House.

Tjulin, A., Eriksson, A. I., & André, M. (2003). Lower hybrid cavities in the inner magnetosphere. *Geophysical Research Letters*, *30*(7), 1364. https://doi.org/10.1029/2003GL016915

Vago, J. L., Kintner, P. M., Chesney, S. W., Arnoldy, R. L., Lynch, K. A., Moore, T. E., & Pollock, C. J. (1992). Transverse ion acceleration by localized lower hybrid waves in the topside auroral ionosphere. *Journal of Geophysical Research*, *97*(A11), 16,935–16,957. https://doi.org/10.1029/92JA01526

Woodroffe, J. R., & Streltsov, A. V. (2013). Whistler propagation in the plasmapause. *Journal of Geophysical Research: Space Physics*, *118*, 716–723. https://doi.org/10.1002/jgra.50135

Xiao, F., Liu, S., Tao, X., Su, Z., Zhou, Q., Yang, C., et al. (2017). Generation of extremely low frequency chorus in Van Allen radiation belts. *Journal of Geophysical Research: Space Physics*, *122*, 3201–3211. https://doi.org/10.1002/2016JA023561